Spin wave spectra of single crystal CoPS3

A. R. Wildes, B. Fåk, U. B. Hansen, M. Enderle, J. R. Stewart, L. Testa, H. M. Rønnow, C. Kim and Je-Geun Park

Published version information

Citation: AR Wildes et al. Spin wave spectra of single crystal CoPS3. Phys Rev B 107, no. 5 (2023): 054438

DOI: 10.1103/PhysRevB.107.054438

Editors' Suggestion

Spin wave spectra of single crystal $CoPS_3$

A. R. Wildes, * B. Fåk, U. B. Hansen, and M. Enderle
Institut Laue-Langevin, 71 avenue des Martyrs CS 20156, 38042 Grenoble Cedex 9, France

J. R. Stewart
ISIS Pulsed Neutron and Muon Source, STFC Rutherford Appleton Laboratory, Harwell Campus, Didcot OX11 0QX, United Kingdom

L. Testa and H. M. Rønnow
Laboratory for Quantum Magnetism, Institute of Physics, École Polytechnique Fédérale de Lausanne (EPFL), CH-1015 Lausanne, Switzerland

C. Kim and Je-Geun Park
Center for Quantum Materials, Seoul National University, Seoul 08826, Korea;
Center for Correlated Electron Systems, Institute for Basic Science, Seoul 08826, Korea;
and Department of Physics and Astronomy, Seoul National University, Seoul 08826, Korea

(Received 9 December 2022; accepted 9 February 2023; published 27 February 2023)

The spin waves in single crystals of the layered van der Waals antiferromagnet $CoPS_3$ have been measured using inelastic neutron scattering. The data show four distinct spin wave branches with large ($\gtrsim$14 meV) energy gaps at the Brillouin zone center indicating significant anisotropy. The data were modeled using linear spin wave theory derived from a Heisenberg Hamiltonian. Exchange interactions up to the third nearest-neighbor in the layered planes were required to fit the data with ferromagnetic $J_1 = -1.37$ meV between first neighbors, antiferromagnetic $J_3 = 3.0$ meV between third neighbors, and a very small $J_2 = 0.09$ meV between second neighbors. A biaxial single-ion anisotropy was required, with a collinear term $D^x = -0.77$ meV for the axis parallel to the aligned moment direction and a coplanar term $D^z = 6.07$ meV for an axis approximately normal to the layered crystal planes.

DOI: 10.1103/PhysRevB.107.054438

I. INTRODUCTION

Magnetic van der Waals compounds have attracted considerable attention as magnetic analogues to graphene [1,2]. These compounds offer possibilities to delaminate down to monolayer thickness and can be intercalated with other atoms and molecules. Of particular interest in this context is the family of (antiferromagnetic) transition-metal compounds $TMPS_3$, with TM = Mn, Fe, Co, or Ni [3–6]. In these compounds, the TM^{2+} ions form a honeycomb lattice in the crystallographic (a, b) planes and have an octahedral coordination with six surrounding sulfur atoms. The composite forms layers that are stacked along the c axis, weakly bound by van der Waals forces, with the resulting structure corresponding to the monoclinic $C2/m$ space group [7].

The quasi-two-dimensionality of the crystal structure extends to the magnetic properties where, even in bulk, the compounds have been investigated as possible model magnetic systems. $CoPS_3$ deserves particular attention as it is a candidate for possible exotic magnetic states. Theory models for $S = 3/2$ on a honeycomb lattice, which is the high-spin state for Co^{2+}, predict a possible valence-bond state [8]. Orbital contributions, also present in Co^{2+}, may perturb such a state, however, the subsequent lifting of the degeneracy in the d^7 orbitals due to spin-orbit and crystal electric field effects combined with lattice distortions may lead to an effective $\mathcal{J}_{\text{eff}} = 1/2$ angular momentum state with associated Kitaev-like physics [9,10]. The compound orders antiferromagnetically below a relatively high Néel temperature of $T_N \approx 120$ K, forming the zigzag antiferromagnetic structure shown in Fig. 1 [11,12]. The structure is similar to other Kitaev-Heisenberg candidates [13] such as Na_2IrO_3 [14], α-$RuCl_3$ [15,16], and the cobalt-containing compounds $Na_3Co_2SbO_6$ and $Na_2Co_2TeO_6$ [17]. Long-ranged magnetic order, which cannot occur in two-dimensional Heisenberg systems according to the Mermin-Wagner theorem [18], is stabilized by a planar anisotropy that is apparent in the paramagnetic susceptibility [12]. The anisotropy is likely associated with orbital contributions but these are relatively small, estimated to be $L \approx 0.32$ based on the effective moment determined from paramagnetic susceptibility ($\mu_{\text{eff}} = 4.55\,\mu_B$ versus $3.87\,\mu_B$ for $g = 2$ and spin-only $S = 3/2$) and the size of the ordered moment ($gS = 3.4\,\mu_B$ versus 3 for $g = 2$ and $S = 3/2$).

However, neutron inelastic scattering experiments on powdered samples provide the clearest evidence that exotic magnetic states are not found in $CoPS_3$ [23,24]. The data indicate that $CoPS_3$ has well-defined spin waves with spectral weight between 15–35 meV. The energy gap is indicative of the relatively large anisotropy. Spectral weight due to a

*wildes@ill.fr

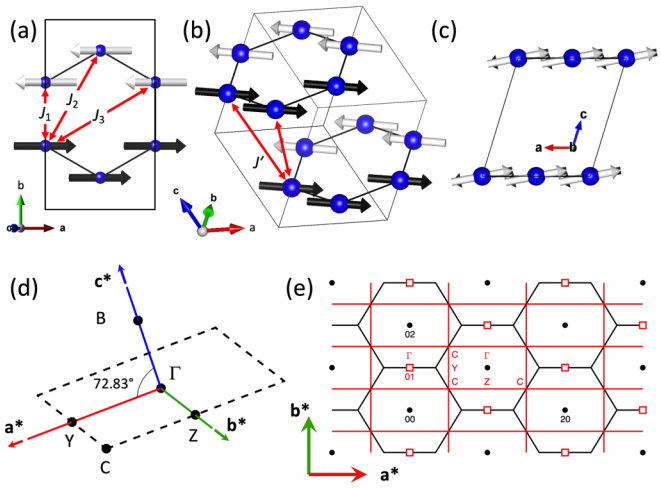

FIG. 1. The magnetic structure of $CoPS_3$ [12], viewed (a) along the $c^\star$ axis, (b) isometrically, and (c) along the b axis. The magnetic exchanges between first, second, and third nearest intraplanar neighbors are labeled in (a) as J_1, J_2, and J_3 respectively, and the exchanges between interplanar nearest neighbors are labeled in (b) as J'. The VESTA software package was used to create the figure [19]. (d) The Brillouin zone for the magnetic structure of $CoPS_3$. Selected high-symmetry points are indicated, corresponding to the magnetic space group P_C2_1/m (#11.57) as defined in the Bilbao Crystallographic Library [20–22]. (e) An $(a^\star, b^\star)$ plane for $CoPS_3$. Brillouin zone boundaries are shown for the crystallographic and magnetic lattices as black and red lines, respectively. Nuclear Brillouin zone centers are shown as black filled circles. Strong magnetic Bragg peaks appear at the red open squares. Selected hk Miller indices and high-symmetry points are indicated.

possible crystal field level was observed at 70 meV [24], but nothing similar appeared at lower energies. The energy scales for the spin wave spectrum are much larger than those observed for the other Kitaev-Heisenberg candidate compounds, and the scattering could be modeled using linear spin wave theory with a larger spin $S = 3/2$. The best model required biaxial anisotropy terms, resulting in the spin wave dispersion having four distinct and nondegenerate branches from the four moments per magnetic unit cell. It was assumed that there was no exchange between the ab planes, and that the magnetism was purely two dimensional.

Powder-averaged data lose the directional information associated with excitation propagation vectors, potentially introducing ambiguity into the modeling. Measurements on single crystals are necessary to verify that the modeling is correct. This paper describes neutron inelastic scattering experiments on coaligned single crystals of $CoPS_3$ to elucidate the spin dynamics. The results confirm the conclusions that $CoPS_3$ has the larger $S = 3/2$ with clear spin waves, and the data are modeled with linear spin wave theory. The results are discussed in the context of the expected electronic configuration of the Co^{2+} in its crystal-symmetry environment.

II. EXPERIMENT AND RESULTS

A. Sample preparation

Single-crystal samples of $CoPS_3$ were grown by direct combination of the pure elements in an evacuated, sealed quartz ampoule using the protocol described in Ref. [12]. The largest crystals, with approximate dimensions $\approx 4 \times 2 \times 0.5$ mm^3, were identified and their crystal quality was verified using x-ray Laue diffraction. The TM-PS_3 compounds are well known to suffer from twinning due to a 120° rotation of the ab planes around the $c^\star$ axis [25]. All the crystals were determined to be better than 75% monodomain using neutron diffraction on the IN3 spectrometer at the ILL, France [26].

IN3 was also used to coalign the crystals. Each crystal was individually wrapped in aluminium foil and then attached to a thin aluminium plate using a small amount of GE varnish. The glue was never in direct contact with the crystals. The normal to the plate was thus coaxial with the $c^\star$ axis, with the crystals aligned to share the same $b^\star$ axis for their majority domains in the plane of the plate.

A coaligned sample with four crystals glued to one plate was used for the neutron three-axis spectrometer measurements. A fifth crystal on a second plate was added for measurements using time-of-flight spectrometry. The two plates were coaligned by mounting them on a common aluminium "toaster rack" support.

B. Unpolarized three-axis spectrometry

Preliminary neutron measurements were performed using the IN8 thermal neutron three-axis spectrometer at the ILL, France [27]. The sample was aligned to measure the scattering in the $(hk0)$ plane. IN8 was configured with a bent silicon 111 monochromator and a horizontally focusing pyrolytic graphite 002 analyzer. Both monochromator and analyzer used vertical focusing. The final wave number was fixed at $k_f = 2.662$ Å^{-1}, and a graphite filter was placed before the analyzer to filter contamination from higher-order λ/n contributions. Temperature control down to 1.5 K was achieved using a liquid helium cryostat.

The measurements confirmed the presence of the energy gap and the band width of the spin wave spectral weight observed in the measurements from powdered samples [23]. However, the scattering appeared to have significant contributions from phonons. Figures 2(a) and 2(b) show the scattering measured at 210 and $\frac{5}{2}10$ corresponding, respectively, to Γ and Y points of the magnetic space group P_C2_1/m (#11.57) shown in Fig. 1(d), in both the magnetically ordered state at 2 K and well above T_N at 150 K. The data have been divided by the temperature factor, $1/(1 - \exp[-E/k_BT])$. Features are visible at both temperatures. The high-temperature data underlie the low-temperature data, indicating bosonlike features whose energies are relatively temperature independent, as expected for phononic contributions.

Magnetic contributions from critical fluctuations can persist to relatively high temperatures above T_N in low-dimensional materials. As seen in sister compounds, however, they are expected to be very broad and at much lower energies, particularly at the Brillouin zone center [28,29]. Thus the high-temperature data, once corrected for the temperature factor, could be taken as a phonon background and were subtracted from the low-temperature data to determine the spin wave contributions. The temperature subtractions are shown in Figs. 2(c) and 2(d). Two clear peaks at ≈15 meV and ≈23 meV are visible at the Γ point. A suggestion of

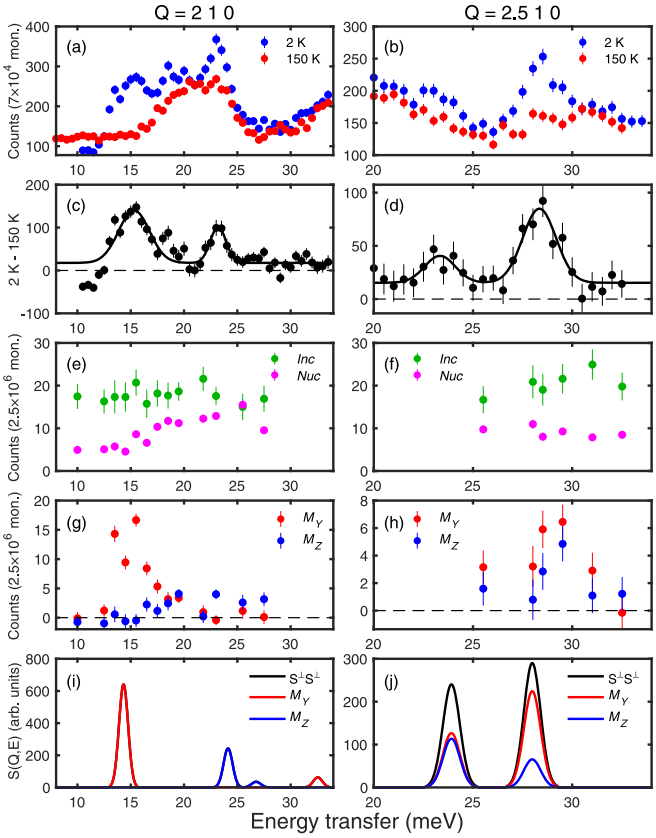

FIG. 2. Neutron three-axis spectroscopy data and simulation for the magnetic excitations in $CoPS_3$ at 210 (left column) and $\frac{5}{2}10$ (right column), corresponding to Γ and Y points respectively. (a) and (b) show measurements from IN8, each with data at 2 K and 150 K. The data have been divided by the temperature factor. The differences between the scattering at the two temperatures are shown in (c) and (d), and the peak positions have been determined by fitting Gaussian functions. (e) - (h) show the separated contributions to the scattering determined from IN20 neutron polarization analysis data using Eq. (1). The nuclear coherent and isotopic incoherent, *Nuc*, and nuclear spin incoherent, *Inc*, contributions are shown in (e) and (f), and the directional components of the magnetic fluctuations, M_Y and M_Z, are shown in (g) and (h). SpinW calculations of the modeled spin waves are shown in (i) and (j). $S^{\perp}$ refers to the components of the spin fluctuations that are perpendicular to the neutron scattering vector, **Q**. Instrument resolution has not been included in the calculations, and the magnons have been broadened by an arbitrary width of 1 meV.

a third peak at 18.5 meV is likely due to a spurious signal as the elastic scattering momentum triangle with the nominal incident wave number at this position closes near to the $2\bar{1}0$ magnetic Bragg peak. Two peaks are also seen at the Y point, at ≈23 meV and ≈28 meV. No clear evidence for spin waves was observed below 14 meV or above 30 meV.

C. Polarized three-axis spectrometry

Neutron polarization analysis is capable of separating the magnetic scattering from other contributions, for example, from phonons, and is furthermore capable of determining the directional components of the magnetic fluctuations. Consequently, the polarized neutron IN20 spectrometer at the ILL, France was used to clarify the measurements performed on IN8.

The same sample orientation as on IN8 was used for the measurements on IN20. Heusler Cu_2MnAl 111 crystals were used for both the polarizing monochromator and analyzer. The final wave number was again fixed at 2.662 $Å^{-1}$ with a graphite filter before the analyzer to suppress higher-order contamination. The neutron polarization direction at the sample position was set using current-carrying coils, and a neutron spin flipper before the analyzer was used to measure different polarization states. A liquid helium cryostat was again used for temperature control.

A total of six polarization states were measured at each (**Q**, ω) point on IN20. Measurements were performed with the flipper on and off with the polarization axis at the sample in one of three orthogonal directions: parallel to **Q** (designated X), in the scattering plane perpendicular to **Q** (Y), and normal to the scattering plane (Z). The measurements with the flipper off and on are designated NSF_P and SF_P respectively for each of the polarization axes $P = X, Y, Z$. Linear combinations of these measurements were used to separate the different contributions to the total scattering [30], with:

$$
\begin{aligned}
Nuc &= \left(2\sum_{P}^{X,Y,Z} NSF_P - \sum_{P}^{X,Y,Z} SF_P\right)\Big/ 6 \\
Inc &= 3(SF_Y + SF_Z - SF_X)/2 \\
M_Y &= (NSF_Y - NSF_X + SF_X - SF_Y)/2 \\
M_Z &= (NSF_Z - NSF_X + SF_X - SF_Z)/2, \qquad (1)
\end{aligned}
$$

where *Nuc* is the nuclear-coherent and isotope-incoherent scattering, *Inc* is the nuclear-spin-incoherent scattering, M_Y and M_Z are the scattering due to the magnetic components along Y and Z, respectively. The isotope-incoherent scattering from $CoPS_3$ and the aluminium mount is negligible [31] and is ignored in subsequent discussion.

Figures 2(e) and 2(f) show the separated nuclear-coherent and nuclear-spin-incoherent contributions at the 210 and $\frac{5}{2}10$ positions, respectively. Both are large. The nuclear-spin-incoherent contribution comes partly from the cobalt, whose incoherent cross section of 4.8 barns/atom [31] is purely due to nuclear spin, and also from the hydrogen in the GE varnish used to glue the crystals. The large nuclear-coherent scattering verifies the conclusion that the IN8 data suffered from phonon contamination. The large phonon density at similar energies to the spin waves may have important ramifications regarding magnetostriction properties of $CoPS_3$.

Figure 2(g) shows the purely magnetic scattering at the Γ point, and may be directly compared to Fig. 2(c). The ≈15 meV peak is clearly seen and is shown to be solely due to fluctuations in the ($hk0$) plane. The ≈23 meV peak and the, probably spurious, peak at ≈18.5 meV are not clearly seen, but the data show fluctuations normal to the ($hk0$) plane at these energies with the intensity above 22 meV being exclusively due to these fluctuations.

Similar measurements at $\frac{5}{2}10$ are shown in Fig. 2(h), which may be compared to the unpolarized data in Fig. 2(d). The measurements concentrated on higher energies. The peak at

≈28 meV is seen and shown to have contributions from magnetic fluctuations both within and normal to the $hk0$ plane, with the former fluctuations giving a larger intensity.

D. Time-of-flight spectrometry

Broad surveys of reciprocal space were measured using the direct geometry time-of-flight spectrometer MAPS at the ISIS facility, UK [32]. The instrument was configured with an incident energy of $E_i = 70$ meV and the S chopper at a frequency of 250 Hz, giving a resolution of $\Delta E \approx 3$ meV and ≈2.2 meV at energy transfers of 15 meV and 35 meV respectively. Temperature control to 5 K was achieved with a closed circuit cryorefrigerator.

The samples were mounted with the $b^\star$ axis oriented vertically and were initially aligned with $c^\star$ parallel to the incident beam. A series of measurements were performed as a function of the rotation about the vertical axis, sweeping $\pm 60^\circ$ about the initial alignment with 1° steps. The data were then combined using MANTID [33] and cuts and slices were then extracted and analyzed using the HORACE software [34].

The data showed clear dispersive features within the energy range determined from measurements on powdered samples [23]. Their intensities decreased with increasing **Q**, as expected for neutron magnetic scattering due to the form factor, and hence they were taken to be due to spin waves. The data had less contamination from nonmagnetic signals than the three-axis measurements, largely as MAPS was able to access smaller **Q** where the phonon signal is small.

Slices parallel to the $c^\star$ axis were extracted to determine whether there was any dispersion due to interplanar interactions, shown in Fig. 3. The scattering was weak, and slices with relatively large widths, ± 0.1 in h and k, were combined at symmetry-equivalent $\{hk\}$ for adequate statistics. There is no clear dispersion along l within the resolution of the binning, showing $CoPS_3$ to be a good approximation of a two-dimensional magnet. The interplanar exchange, J', was thus set to be zero for the rest of the analysis. A dedicated experiment with better statistics and resolution will be required to determine the size of J'.

Data could thus be integrated along l to improve statistics. Symmetry-equivalent slices were also combined to improve statistics further. Figure 4 shows slices parallel to the $a^\star$ axis, integrated for $0 \leqslant l \leqslant 2$ and centered at different k. Figure 5 shows similarly binned slices parallel to the $b^\star$ axis centered at different h. The dispersive modes are clearly visible, and slice trajectories may be mapped onto the $(a^\star, b^\star)$ plane shown in Fig. 1(e). Although the 210 and $\frac{5}{2}10$ positions measured using three-axis spectrometers were inaccessible using the MAPS configuration, the slices contain numerous other symmetry-equivalent points.

Data at integer values of h in Figs. 4(a) and 4(e) correspond to Γ points, and likewise at integer k in Figs. 5(a) and 5(e). Modes at ≈15 meV and ≈23 are again observed, for example at $(h, k) = (1, 2)$, which is also a strong magnetic Bragg peak position. A further two higher-energy modes are observed at positions such as $(h, k) = (0, 2)$ and $(1, 1)$. These modes are strongest at silent magnetic Bragg peak positions. No peak is observed at 18.5 meV, supporting the conclusion that this is a spurious feature in the IN8 data. Thus, a total of four spin

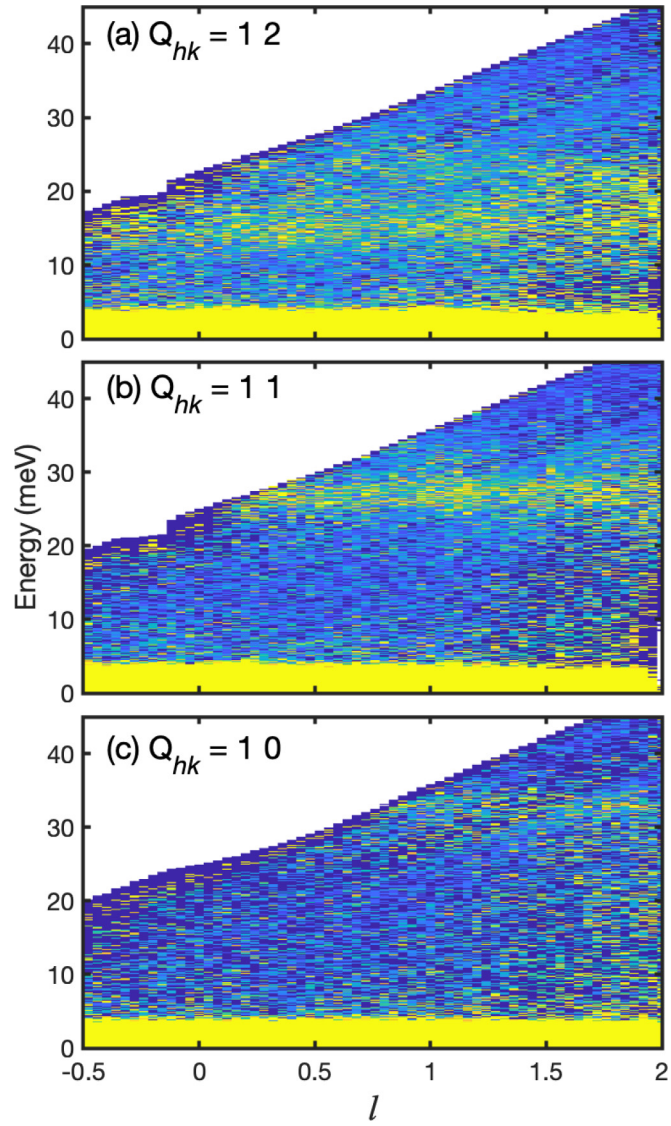

FIG. 3. Neutron inelastic scattering data from MAPS for slices parallel to the $c^\star$ axis, collected at 5 K. Equivalent reciprocal lattice points were shown to be qualitatively the same and the data have been combined for better statistics. The trajectories have fixed $\{hk\}$ of (a) {12}, (b) {11}, and (c){10}, thus incorporating Brillouin zone centres. The slice widths are ± 0.1 in both h and k.

wave modes are present at the Brillouin zone center, consistent with the conclusions from the analysis of neutron inelastic scattering from powdered samples [23].

Data at half-integer h in Figs. 4(a) and 4(e), and at integer k in Fig. 5(c), correspond to Y points in the Brillouin zone and may be compared with Figs. 2(b) and 2(h). The MAPS data confirm the presence of the two modes observed on IN8, and show that these are the only two modes at this position. The observations are again consistent with the previous analysis [23].

The individual slices for all the combined data in Figs. 3–5 were examined prior to being combined and were shown to be qualitatively the same. No artifacts due to crystal twinning were observed, reflecting the quality and alignment of the

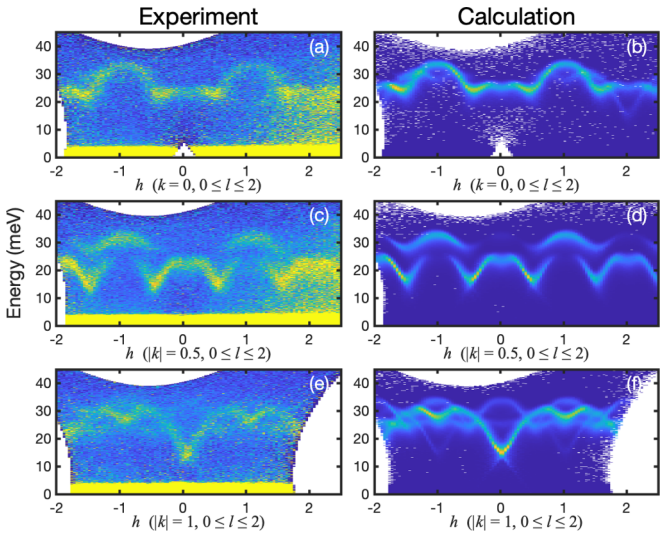

FIG. 4. Neutron inelastic scattering data from MAPS for slices parallel to the $a^\star$ axis, collected at 5 K. Data and models have been integrated for $0 \leqslant l \leqslant 2$. Slices centered at $\pm k$ were shown to be equivalent and have been combined for statistics with a slice width of $|k| \pm 0.1$. Slices along (a) $h0$, (c) $h|\frac{1}{2}|$, and (e) $h|1|$ are shown with corresponding calculations in (b), (d), and (f).

crystals chosen for the experiment, and twinning effects were ignored in the subsequent data analysis.

III. ANALYSIS WITH LINEAR SPIN WAVE THEORY

The experimental results showed well-defined and dispersive excitations at relatively large energies, consistent with a spin wave picture. The neutron scattering could thus be fitted and modeled using linear spin wave theory. The dynamic

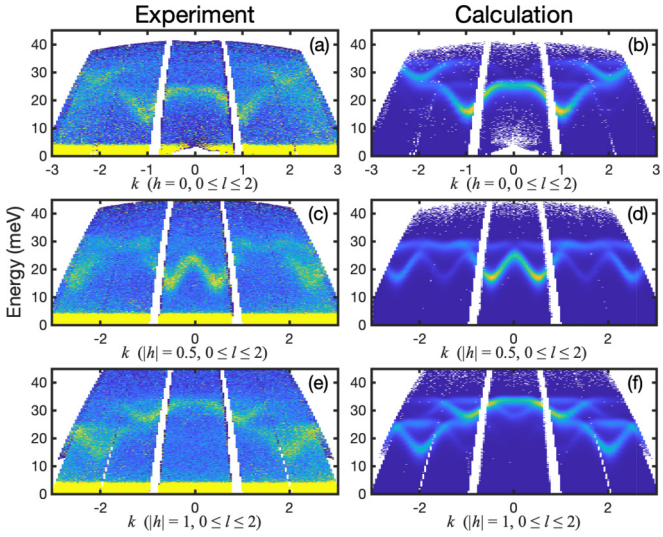

FIG. 5. Neutron inelastic scattering data from MAPS for slices parallel to the $b^\star$ axis, collected at 5 K. Data and models have been integrated for $0 \leqslant l \leqslant 2$. Slices centered at $\pm h$ were shown to be equivalent and have been combined for statistics with a slice width of $|h| \pm 0.1$. Slices along (a) $0k$, (c) $|\frac{1}{2}|k$, and (e) $|1|k$ are shown with corresponding calculations in (b), (d), and (f).

TABLE I. The analytic expressions for the eigenvalues at specific points in the Brillouin zone, as given by SPINW. The label for each high-symmetry point, as defined in Fig. 1(d), is listed beside its reduced lattice position. The two or four modes at each point are numbered. The parameters D^x and D^z are taken to be always negative, for uniaxial anisotropy, and positive, for planar anisotropy, respectively. The parameters U and V for the eigenvalues at the Z point are defined in Eqs. (A1) and (A2)

Γ	0 0 0
1:	$2S(2D^x(D^x - D^z - J_1 - 4J_2 - 3J_3))^{\frac{1}{2}}$
2:	$2S((D^x - D^z)(2D^x - J_1 - 4J_2 - 3J_3))^{\frac{1}{2}}$
3:	$2S((D^x - D^z + 2J_1 - 4J_2 + 2J')(2D^x + J_1 - 3J_3 + 2J'))^{\frac{1}{2}}$
4:	$2S(2(D^x + J_1 - 2J_2 + J')(D^x - D^z + J_1 - 3J_3 + 2J'))^{\frac{1}{2}}$
Y	$\frac{1}{2}00$
1:	$2S((2D^x - J_3 + J')(D^x - D^z + J_1 - 2J_3 + J'))^{\frac{1}{2}}$
2:	$2S((D^x - D^z - J_3 + J')(2D^x + J_1 - 2J_3 + J'))^{\frac{1}{2}}$
Z	$0\frac{1}{2}0$
1:	$S(2U - 2(V)^{\frac{1}{2}})^{\frac{1}{2}}$
2:	$S(2U + 2(V)^{\frac{1}{2}})^{\frac{1}{2}}$
C	$\frac{1}{2}\frac{1}{2}0$
1:	$2S((2D^x + J')(D^x - D^z + J_1 - 3J_3 + J'))^{\frac{1}{2}}$
2:	$2S((D^x - D^z + J')(2D^x + J_1 - 3J_3 + J'))^{\frac{1}{2}}$
B	$00\frac{1}{2}$
1:	$2S((D^x - D^z + 4J')(D^x - J_1 - 4J_2 - 3J_3 + 4J'))^{\frac{1}{2}}$
2:	$2S((D^x + 4J')(D^z - D^x - J_1 - 4J_2 - 3J_3 + 4J'))^{\frac{1}{2}}$
3:	$2S((D^x - D^z + 2J_1 - 4J_2 + 2J')(D^x + J_1 - 3J_3 + 2J'))^{\frac{1}{2}}$
4:	$2S((D^x + 2J_1 - 4J_2 + 2J')(D^x - D^z + J_1 - 3J_3 + 2J'))^{\frac{1}{2}}$

structure factor, $S(\mathbf{Q}, \omega)$, was derived from a Hamiltonian using isotropic exchange parameters, J_{ij} between moments i and j, and two single-ion anisotropies, D^x and D^z:

$$\hat{\mathcal{H}} = \frac{1}{2}\sum_{\langle ij \rangle} J_{ij}\left(S_i^x S_j^x + S_i^y S_j^y + S_i^z S_j^z\right) + D^x \sum_i \left[\left(S_i^x\right)^2 - \left(S_i^y\right)^2\right] + D^z \sum_i \left(S_i^z\right)^2, \quad (2)$$

where the x axis is collinear with the aligned moment axis, the y axis is parallel to the crystallographic b axis, and z is perpendicular to both x and y. The single-ion anisotropy is thus biaxial, with negative/positive $D^{x,z}$ defining an easy-axis/plane, respectively.

$CoPS_3$ has four magnetic atoms per monoclinic unit cell. The Hamiltonian is thus expressed as an 8×8 matrix, which is not easily diagonalized analytically for an arbitrary reduced reciprocal lattice vector. The SPINW software package for MATLAB® [35] can provide analytical expressions for the spin wave energies when it is used with the MATLAB® symbolic toolbox, however, it was not able to provide general expressions in a reasonable time. It was, though, able to provide analytical expressions from Eq. (2) at specific high-symmetry points in the Brillouin zone. The expressions are listed in Table I.

The xyz axes in Eq. (2) are defined with respect to the spin direction and, with the exception of y, are not linked

TABLE II. The data points, eigenvalues, and fitted parameters. The eigenvalue numbering is defined with respect to the order in Table I. All energies are in meV.

Q	k vector	Eigenvalue	Measured energy	Fitted energy
0 1	Γ	1	14.5(1)	14.28
1 2	Γ	1	14.9(3)	”
0 0	Γ	2	23.0(2)	24.13
2 0	Γ	2	21.4(3)	”
1 2	Γ	2	23.6(3)	”
1 0	Γ	3	31.8(2)	32.56
0 1	Γ	3	32.3(5)	”
0 2	Γ	4	26.4(2)	26.75
1 1	Γ	4	26.6(2)	”
$\frac{1}{2}$0	*Y*	1	23.3(1)	24.01
$\frac{3}{2}$1	*Y*	1	23.4(2)	”
$\frac{3}{2}$1	*Y*	2	29.6(2)	28.01
0$\frac{1}{2}$	*Z*	1	22.0(1)	21.89
0$\frac{3}{2}$	*Z*	1	22.1(3)	”
1$\frac{3}{2}$	*Z*	1	22.2(1)	”
1$\frac{5}{2}$	*Z*	1	21.9(1)	”
0$\frac{3}{2}$	*Z*	2	30.8(3)	30.90
1$\frac{3}{2}$	*Z*	2	31.0(2)	”
1$\frac{1}{2}$	*Z*	2	31.2(1)	”
$\frac{1}{2}\frac{1}{2}$	*C*	1	15.1(1)	15.39
$\frac{3}{2}\frac{1}{2}$	*C*	1	15.5(1)	”
$\frac{3}{2}\frac{1}{2}$	*C*	2	27.1(2)	27.0
$\frac{3}{2}\frac{3}{2}$	*C*	2	28.5(2)	”

to the crystallographic axes. The equations in Table I are unchanged for any moment direction in the (a, c) plane. The magnetic structure for $CoPS_3$ has a small out-of-plane tilt of $\approx 9.5^\circ$ with respect to the crystallographic a axis, but this was neglected in the SPINW data analysis and the moments were assumed to lie along a such that x and a are collinear, as are the z and $c^\star$ axes. The assumption made no difference when calculating the spin wave energies, but impacts calculations for the neutron intensity, which is given by those components of the moments that are perpendicular to the scattering vector **Q**. The impact, however, was small enough to be negligible.

Energy cuts at the high-symmetry points were extracted from the experimental data. The data showed clear peaks which were fitted with Gaussians to determine the spin wave energies. The resulting energies, with their corresponding **Q**, are listed in Table II.

The energies at each high-symmetry point were attributed to appropriate eigenvalue equations, and then the ensemble was fitted with common parameters for the exchanges and anisotropies. The attribution of the eigenvalue equations may seem arbitrary at first glance, however, different attribution combinations quickly showed that only one gave results consistent with the data. The eigenvalue attribution and fitted energies are also shown in Table II.

The best-fit exchange and anisotropy parameters are listed in Table III. A comparison with calculated mean-field stability conditions for magnetic ground states [36,37] shows that the exchange parameters will give a zigzag antiferromagnetic

TABLE III. The fitted exchange parameters from the current data, and from previous analysis of neutron spectroscopy data from a powdered sample [23]. Negative J denotes a ferromagnetic exchange. D^x and D^z are the magnitudes of the single ion anisotropies along the a and $c^\star$ axes respectively. A negative D denotes a uniaxial anisotropy, and a positive value denotes a planar anisotropy. All exchange parameters and anisotropies are given in meV.

	Current work	Ref. [23]
S	1.5	1.5
J_1	−1.37(7)	−2.04
J_2	0.09(5)	−0.26
J_3	3.0(1)	4.21
α	–	0.6
J'	0	0
D^x	−0.77(3)	−2.06
D^z	6.07(4)	–

structure, as expected for $CoPS_3$. Exchange interactions up to the third neighbor in the ab plane, shown in Fig. 1(a), were required to give an adequate fit, which is consistent with similar conclusions for $MnPS_3$ [38], $FePS_3$ [39] and $NiPS_3$ [40]. Also consistently with the other members of the family, the second-neighbor exchange, J_2, is very small, while J_3 is quite large and antiferromagnetic. The first-neighbor exchange, J_1, is ferromagnetic, as is the case in $FePS_3$ and $NiPS_3$, and it is the large J_3 that stabilises the antiferromagnetic zigzag order. The anisotropy energies, $D^{x,z}$, are large. D^z is positive, defining the (a, b) plane to be easy, while the negative D^x defines an easy direction in the plane parallel to the ordered collinear moments. This differs to $MnPS_3$ and $FePS_3$, which can be modeled using only an easy-axis single-ion anisotropy. It is similar to $NiPS_3$, which has the same magnetic structure with almost the same moment orientations, albeit having a much smaller D^x/D^z ratio [40].

SPINW is able to numerically diagonalize the Hamiltonian for arbitrary **Q**, subsequently calculating the directional components of the magnetic fluctuations and the expected neutron scattering intensity. The calculated scattering for the IN8 and IN20 measurements is shown in Figs. 2(i) and 2(j). Instrument resolution has not been included in the calculations, whose widths have been broadened by an arbitrary $\Delta E = 1$ meV, and thus the calculations serve primarily as a verification for the modeling of the spin wave energies and directional components. The $S^\perp S^\perp$ calculations represent those fluctuations perpendicular to **Q**, which compare directly and favorably with the unpolarized IN8 data in Figs. 2(c) and 2(d). The directional components for the spin fluctuations in and normal to the scattering plane are shown in Figs. 2(i) and 2(j) as M_Y and M_Z, respectively, agreeing broadly with the IN20 data in Figs. 2(g) and 2(h).

SPINW is also compatible with HORACE [34] and the combined software can be used to calculate the expected neutron scattering, including a convolution with the instrumental resolution. Once the spin wave energies in Table II were fitted and the best estimates for J and $D^{x,z}$ were determined, the combined software was used to calculate the expected neutron scattering for a series of slices through the experimental data using an isotropic $g = 2$. The calculations are remarkably

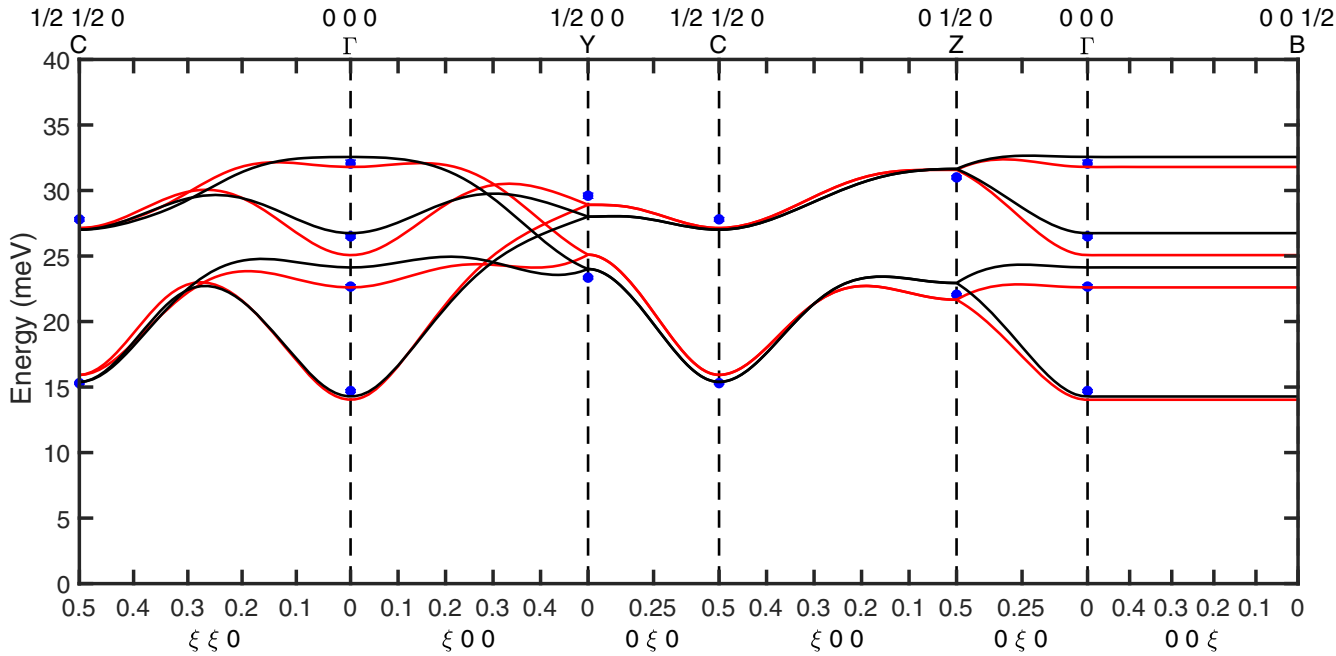

FIG. 6. The spin wave dispersions calculated with the fitted exchange parameters for $CoPS_3$. The red lines show the dispersion using the parameters from Kim *et al.* [23], derived from fitting neutron data from powders using Eq. (3), while the black lines show the results from the current work using Eq. (2). The data points at the high-symmetry positions correspond to an average of the fitted spin wave energies for each of the equivalent eigenvalues listed in Table II.

similar to the experimental data, and are shown beside the corresponding slices in Figs. 4 and 5.

IV. DISCUSSION

The analysis presented in Sec. III differs slightly from the previous analysis of the neutron data from powdered $CoPS_3$ [23], however, the conclusions are coherent. The best fits to the powder data used a Hamiltonian with a combination of a spin-direction-dependent anisotropic exchange with a single-ion term:

$$\hat{\mathcal{H}} = \frac{1}{2}\sum_{\langle ij\rangle} J_{ij}\left(S_i^x S_j^x + S_i^y S_j^y + \alpha S_i^z S_j^z\right) + D^x \sum_i \left(S_i^x\right)^2, \quad (3)$$

where the definitions for the axes xyz are the same as for Eq. (2). An easy-plane anisotropy is obtained by the exchange anisotropy parameter $\alpha < 1$ in Eq. (3) or $D^z > 0$ in Eq. (2). A negative D^x creates a uniaxial anisotropy along the aligned moment direction in both Eqs. (2) and (3), but the magnitudes will differ by a factor 2 as, for symmetry reasons, the relevant single-ion term in Eq. (2) includes a hard axis along the y direction.

Phenomenologically, the choice of Hamiltonian is somewhat arbitrary as, for appropriate parameters, Eqs. (2) and (3) can be used to fit the data with equivalent quality. For comparison, the parameters determined from analyzing the neutron powder data are included in Table III [23]. The calculated spin wave dispersions for both sets of parameters are shown in Fig. 6 along with data points derived from appropriate averages of the fitted energies in Table II. The two sets of parameters give very similar results, thus the experimental results and analysis on single crystals of $CoPS_3$ confirm the conclusions from the previous work on powdered samples. Equation (2) has an advantage that SPINW could give compact analytic expressions for the spin wave energies, shown in Table I, in a reasonable time, which was not the case for Eq. (3). Further motivation for using Eq. (2) to model the data comes from considering the electronic ground state of the Co^{2+} ions.

The most important point regarding the spin dynamics in $CoPS_3$ concerns the absence of a Kramers-doublet ground state arising from an effective $\mathcal{J}_{\text{eff}} = 1/2$ angular momentum state that might be expected from a d^7 ion in an octahedral environment [9,10]. A pertinent discussion has been presented by Winter [41] involving the influence of the crystal electric field and spin-orbit coupling. The crystal field of the octahedral environment of the S^{2-} ions in $CoPS_3$ splits the $3d$ orbitals of Co^{2+} into a low-energy threefold degenerate t_{2g} orbital and a high-energy double-degenerate e_g orbital with zero orbital momentum, split by a large energy expected to be of order $\approx$1 eV. The octahedra in $CoPS_3$ are distorted, having a trigonal elongation along the $c^\star$ axis [7,12,23], which further splits the t_{2g} orbital into a singlet a_{1g} with zero orbital momentum and, at a lower energy proportional to a term Δ_2, a doublet e_g^π. The $3d^7$ electrons of the Co^{2+} fully fill the e_g^π doublet and leave one unpaired electron in the a_{1g} singlet and one in each e_g orbital, giving a high-spin $S = 3/2$ with a quenched orbital moment. The spin-orbit coupling must thus be considered in second order. Furthermore, if the strength of the spin-orbit coupling, λ, is small compared to Δ_2, i.e., $\Delta_2/\lambda \gg 1$, the $\mathcal{J}_{\text{eff}} = 1/2$ and $\mathcal{J}_{\text{eff}} = 3/2$ states merge and the net effect can be considered as a residual easy-plane single-ion anisotropy. The picture is supported by DFT calculations and orbital-filling considerations [42], which correctly reproduced the zigzag $\mathbf{k}_{\text{M}} = [010]$ antiferromagnetic structure for $CoPS_3$ with the preferred moment direction perpendicular to the $c^\star$ axis.

Equation (2) with isotropic exchange and a dominant easy-plane anisotropy provides, hence, a more natural description in view of the electronic ground state of Co^{2+} in $CoPS_3$. The anisotropic exchange parameters in Eq. (3) are appropriate for an effective $\mathcal{J}_{\rm eff} = 1/2$ angular momentum state, which would be expected for an undistorted or a trigonally compressed octahedron and which could result in much sought-after Kitaev coupling. $CoPS_3$ does not have this state, rather having an orbital singlet ground state, and hence the spin-orbit coupling results in a second-order perturbation to a single-ion anisotropy and an anisotropic g tensor.

The conclusion that the Co^{2+} forms an orbital singlet due to the distortion is further reinforced as the Co^{2+} ions have a monoclinic symmetry, lower than the trigonally distorted octahedra, for which all orbital states are singlets. This lower symmetry is important to explain the anisotropy, as trigonally distorted octahedra have a planar symmetry about the quantization axis and will not give rise to the biaxial anisotropy required to fit the $CoPS_3$ spectra.

Estimates for Stevens parameters have been previously calculated for $CoPS_3$ with the appropriate local symmetry for the Co^{2+} ions using first-order perturbation for spin $S = 3/2$ [12]. The calculations were based on the measured asymmetry in the paramagnetic susceptibility and assumed a purely planar anisotropy. When $c^\star$ is defined as quantization axis z, as is the case with the current analysis, Eq. (12) of Ref. [12] gives the traceless anisotropy tensor

$$\mathsf{D} = \begin{bmatrix} 2A_2^0 & 0 & 0 \\ 0 & 2A_2^0 & 0 \\ 0 & 0 & -4A_2^0 \end{bmatrix} = \begin{bmatrix} -1.84 & 0 & 0 \\ 0 & -1.84 & 0 \\ 0 & 0 & 3.76 \end{bmatrix} \tag{4}$$

in units of meV. The values for D^x and D^z in Table III lead to the anisotropy matrix:

$$\tilde{\mathsf{D}} = \begin{bmatrix} D^x & 0 & 0 \\ 0 & -D^x & 0 \\ 0 & 0 & D^z \end{bmatrix}. \tag{5}$$

This can be transformed to a traceless matrix by subtracting $\frac{1}{3}\mathrm{Tr}(\tilde{\mathsf{D}})\mathsf{I}$, where I is the identity matrix. Such an operation has no effect on the Hamiltonian other than an overall energy shift. The result is

$$\mathsf{D} = \begin{bmatrix} -2.79 & 0 & 0 \\ 0 & -1.25 & 0 \\ 0 & 0 & 4.04 \end{bmatrix}, \tag{6}$$

which compares favorably to Eq. (4). The signs for the matrix elements correspond, and the agreement between the $(S^z)^2$ matrix elements is particularly satisfactory. The differences between the $(S^x)^2$ and $(S^y)^2$ matrix elements of Eq. (6) reflects the in-plane anisotropy that was not accounted for in the analysis of the susceptibility data. The crystal field levels have not been comprehensively measured in $CoPS_3$, although neutron spectroscopy data suggest a feature at 70 meV [24]. Future experiments are necessary to fully map the crystal fields.

As previously mentioned, the spin-orbit coupling in second-order perturbation leads to an anisotropy in the g factors [41]. Previous efforts to quantify g have focused on electron spin resonance (ESR) measurements of Co^{2+} substituted in $CdPS_3$ [43,44]. The analysis was based on an effective spin $S_{\rm eff} = 1/2$ and found $g_\parallel \approx 5$ and $g_\perp \approx 4$ for fields parallel to and perpendicular to $\mathbf{c}^\star$, respectively [45]. Reanalyzing the data with $S = 3/2$ has no effect on $g_\parallel$, but halves $g_\perp$ to become ≈ 2 [43]. These values are similar to the predictions from theory, giving $g_\parallel \approx 4$ and $g_\perp \approx 2$ in the limit that Δ_2/λ is large [41]. Further evidence for $g_\parallel > 2$ comes from the sizes of effective moment determined from the paramagnetic susceptibility and from the ordered moment determined by neutron diffraction [12], which are slightly larger than expected for spin only and $g = 2$.

The value for g does not affect the spin wave energies, but does affect the calculated neutron scattering intensity. The calculations in Figs. 2, 4, and 5 used an isotropic $g = 2$ and $S = 3/2$. The agreement between calculation and data is satisfactory, which implies that g in $CoPS_3$ may be more isotropic than expected from the theory and the ESR results. The two conclusions are not necessarily contradictory. The theory and the ESR results consider local moments, which is appropriate for dilute substitution in a $CdPS_3$ matrix as the Co^{2+} ions may be treated as isolated impurities. $CoPS_3$ is much more concentrated and the influence of the molecular field on the electronic states must also be considered, especially as the exchange parameters in Table III are relatively large and must be considered up to the third neighbor in plane. The molecular field term may cause the g factor to become more isotropic. A full treatment of $CoPS_3$, along with other members of the TM-PS_3 family, will be considered in future work.

V. CONCLUSIONS

Neutron inelastic scattering has been used to measure the spin wave spectrum of $CoPS_3$. Four clear and dispersive spin wave branches were observed, and the data could be fitted with a model derived from a Hamiltonian with isotropic exchange interactions and a biaxial single-ion anisotropy. The data are consistent with the results and conclusions of previous neutron spectroscopy data from powdered samples. Exchange interactions up to the third in-plane neighbor needed to be included in the fitting, with resulting values of -1.37 meV, 0.09 meV, and 3.0 meV for first, second, and third neighbors, respectively. The anisotropy was defined by an easy-plane term and an easy-axis term within the plane with values of 6.07 meV and -0.77 meV, respectively. The results are consistent with high-spin $S = 3/2$ spin waves, which may be understood based on the effects of the low point symmetry of the Co^{2+} sites on the crystal electric field levels and the strength and range of the exchange.

ACKNOWLEDGMENTS

We thank the Institut Laue-Langevin, experiments No. TEST-3025 [26], No. 4-01-1632 [27], and No. 4-01-1651 [46] for the allocation of neutron beam time. Experiments at the ISIS Neutron and Muon Source were supported by a beam time allocation RB2010386 [47] from the Science and Technology Facilities Council. We also thank Dr. A. Piovano and Dr. A. Ivanov, F. Charpenay, and V. Gaignon for assistance with the IN8 experiment. and Dr. R. Ewings and Dr. M. D. Le

for their assistance with SPINW and HORACE. A.R.W. sincerely thanks Dr. C. Stock, Dr. M. Zhitomirsky, and Dr. R. Ballou for enlightening discussions. We acknowledge the Swiss National Science Foundation (SNSF) for financial support under Grant No. 188648. Work at Seoul National University was supported by the Leading Researcher Program of the National Research Foundation of Korea (Grant No. 2020R1A3B2079375).

APPENDIX A: EXPRESSIONS FOR U AND V

The expressions for the variables U and V, used to calculate the spin wave energies at the Z points in Table I, are

$$\begin{aligned} U =& (D^x - D^z)(2D^x + J_1 - 4J_2 - 3J_3 + 2J') \\ &+ 2D^x(D^x - D^z + J_1 - 4J_2 - 3J_3 + 2J') \\ &+ 2J_1^2 + 8J_2^2 + 4J_3^2 + 4J'^2 - 4J_1J_2 - 4J_1J_3 + 6J_1J' \\ &+ 12J_2J_3 - 8J_2J' - 6J_3J' \end{aligned} \tag{A1}$$

and

$$\begin{aligned} V =& 2D^x(D^x - D^z)(4J_1 + 4J')^2 \\ &+ (D^x - D^z)^2((J_1 + J_3)^2 + 4(J_1 + J')^2) \\ &+ 8(3D^x - Dz)(J_1 + J')^2(J_1 - 4J_2 - 3J_3 + 2J') \\ &- 16\big(2J_1^3J_2 + 2J_1^3J_3 - J_1^3J' - 4J_1^2J_2^2 - 6J_1^2J_2J_3 \\ &+ 8J_1^2J_2J' - 2J_1^2J_3^2 + 7J_1^2J_3J' - 3J_1^2J'^2 \\ &- 8J_1J_2^2J' - 12J_1J_2J_3J' + 10J_1J_2J'^2 - 4J_1J_3^2J' \\ &+ 8J_1J_3J'^2 - 3J_1J'^3 - 4J_2^2J'^2 - 6J_2J_3J'^2 \\ &+ 4J_2J'^3 - 2J_3^2J'^2 + 3J_3J'^3 - J'^4\big). \end{aligned} \tag{A2}$$

[1] J. G. Park, Opportunities and challenges of 2D magnetic van der Waals materials: Magnetic graphene? J. Phys.: Condens. Matter **28**, 301001 (2016).

[2] H. Li, S. Ruan, and Y.-J. Zeng, Intrinsic van der Waals magnetic materials from bulk to the 2d limit: New frontiers of spintronics, Adv. Mater. **31**, 1900065 (2019).

[3] R. Brec, Review on structural and chemical properties of transition metal phosphorus trisulfides MPS_3, Solid State Ionics **22**, 3 (1986).

[4] V. Grasso and L. Silipigni, Low-dimensional materials: The MPX_3 family, physical features and potential future applications, Riv. Nuovo Cimento **25**, 1 (2002).

[5] M. A. Susner, M. Chyasnavichyus, M. A. McGuire, P. Ganesh, and P. Maksymovych, Metal thio- and selenophosphates as multifunctional van der Waals layered materials, Adv. Mater. **29**, 1602852 (2017).

[6] M. Zhu, H. Kou, K. Wang, H. Wu, D. Ding, G. Zhou, and S. Ding, Promising functional two-dimensional lamellar metal thiophosphates: synthesis strategies, properties and applications, Mater. Horiz. **7**, 3131 (2020).

[7] G. Ouvrard, R. Brec, and J. Rouxel, Structural determination of some MPS_3 layered phases (M = Mn, Fe, Co, Ni and Cd), Mater. Res. Bull. **20**, 1181 (1985).

[8] I. Affleck, T. Kennedy, E. H. Lieb, and H. Tasaki, Rigorous Results on Valence-Bond Ground States in Antiferromagnets, Phys. Rev. Lett. **59**, 799 (1987).

[9] H. Liu and G. Khaliullin, Pseudospin exchange interactions in d^7 cobalt compounds: Possible realization of the Kitaev model, Phys. Rev. B **97**, 014407 (2018).

[10] R. Sano, Y. Kato, and Y. Motome, Kitaev-Heisenberg Hamiltonian for high-spin d^7 Mott insulators, Phys. Rev. B **97**, 014408 (2018).

[11] G. Ouvrard, R. Brec, and J. Rouxel, Synthesis and physical characterisation of the lamellar compound $CoPS_3$, C. R. Acad. Sci. Paris Ser. II **t.294**, 971 (1982).

[12] A. R. Wildes, V. Simonet, E. Ressouche, R. Ballou, and G. J. McIntyre, The magnetic properties and structure of the quasi-two-dimensional antiferromagnet $CoPS_3$, J. Phys.: Condens. Matter **29**, 455801 (2017).

[13] S. Trebst and C. Hickey, Kitaev materials, Phys. Rep. **950**, 1 (2022).

[14] S. K. Choi, R. Coldea, A. N. Kolmogorov, T. Lancaster, I. I. Mazin, S. J. Blundell, P. G. Radaelli, Y. Singh, P. Gegenwart, K. R. Choi, S.-W. Cheong, P. J. Baker, C. Stock, and J. Taylor, Spin Waves and Revised Crystal Structure of Honeycomb Iridate Na_2IrO_3, Phys. Rev. Lett. **108**, 127204 (2012).

[15] J. A. Sears, M. Songvilay, K. W. Plumb, J. P. Clancy, Y. Qiu, Y. Zhao, D. Parshall, and Y.-J. Kim, Magnetic order in $\alpha - RuCl_3$: A honeycomb-lattice quantum magnet with strong spin-orbit coupling, Phys. Rev. B **91**, 144420 (2015).

[16] C. Ritter, Zigzag type magnetic structure of the spin $J_{\text{eff}} = 1/2$ compound α-$RuCl_3$ as determined by neutron powder diffraction, J. Phys.: Conf. Ser. **746**, 012060 (2016).

[17] C. Kim, J. Jeong, G. Lin, P. Park, T. Masuda, S. Asai, S. Itoh, H.-S. Kim, H. Zhou, J. Ma, and J.-G. Park, Antiferromagnetic Kitaev interaction in $J_{\text{eff}} = 1/2$ cobalt honeycomb materials $Na_3Co_2SbO_6$ and $Na_2Co_2TeO_6$, J. Phys.: Condens. Matter **34**, 045802 (2021).

[18] N. D. Mermin and H. Wagner, Absence of Ferromagnetism or Antiferromagnetism in One- or Two-Dimensional Isotropic Heisenberg Models, Phys. Rev. Lett. **17**, 1133 (1966).

[19] K. Momma and F. Izumi, VESTA 3 for three-dimensional visualization of crystal, volumetric and morphology data, J. Appl. Crystallogr. **44**, 1272 (2011).

[20] M. I. Aroyo, J. M. Perez-Mato, D. Orobengoa, E. Tasci, G. de la Flor, and A. Kirov, Crystallography online: Bilbao Crystallographic Server, Bulg. Chem. Commun. **43**, 183 (2011).

[21] M. I. Aroyo, J. M. Perez-Mato, C. Capillas, E. Kroumova, S. Ivantchev, G. Madariaga, A. Kirov, and H. Wondratschek, Bilbao crystallographic server: I. databases and crystallographic computing programs, Z. Kristallogr. **221**, 15 (2006).

[22] M. I. Aroyo, A. Kirov, C. Capillas, J. M. Perez-Mato, and H. Wondratschek, Bilbao Crystallographic Server. II. Representations of crystallographic point groups and space groups, Acta Crystallogr. A **62**, 115 (2006).

[23] C. Kim, J. Jeong, P. Park, T. Masuda, S. Asai, S. Itoh, H.-S. Kim, A. Wildes, and J.-G. Park, Spin waves in the

two-dimensional honeycomb lattice xxz-type van der waals antiferromagnet $CoPS_3$, Phys. Rev. B **102**, 184429 (2020).

[24] C. Kim, H.-S. Kim, and J.-G. Park, Spin-orbital entangled state and realization of Kitaev physics in 3d cobalt compounds: A progress report, J. Phys.: Condens. Matter **34**, 023001 (2022).

[25] C. Murayama, M. Okabe, D. Urushihara, T. Asaka, K. Fukuda, M. Isobe, K. Yamamoto, and Y. Matsushita, Crystallographic features related to a van der Waals coupling in the layered chalcogenide $FePS_3$, J. Appl. Phys. **120**, 142114 (2016).

[26] L. Testa, V. Favre, and A. Wildes, Alignment of $CoPS_3$ crystals (2019), doi: 10.5291/ILL-DATA.TEST-3025.

[27] A. Wildes, B. Fåk, U. B. Hansen, and L. Testa, The spin wave spectrum of $CoPS_3$ (2019), doi: 10.5291/ILL-DATA.4-01-1632.

[28] A. R. Wildes, H. M. Rønnow, B. Roessli, M. J. Harris, and K. W. Godfrey, Static and dynamic critical properties of the quasi-two-dimensional antiferromagnet $MnPS_3$, Phys. Rev. B **74**, 094422 (2006).

[29] A. R. Wildes, K. C. Rule, R. I. Bewley, M. Enderle, and T. J. Hicks, The magnon dynamics and spin exchange parameters of $FePS_3$, J. Phys.: Condens. Matter **24**, 416004 (2012).

[30] R. M. Moon, T. Riste, and W. C. Koehler, Polarization analysis of thermal-neutron scattering, Phys. Rev. **181**, 920 (1969).

[31] V. F. Sears, Neutron scattering lengths and cross sections, Neutron News **3**, 26 (1992).

[32] T. G. Perring, A. D. Taylor, R. Osborn, D. M. Paul, A. T. Boothroyd, and G. Aeppli, *Proceedings of the 12th Meeting of the International Collaboration on Advanced Neutron Sources (ICANS XII), Cosener's House, Abingdon, Oxfordshire, 24–28 May, 1993* (RAL, Didcot, 1994), pp. I–60.

[33] O. Arnold, J. C. Bilheux, J. M. Borreguero, A. Buts, S. I. Campbell, L. Chapon, M. Doucet, N. Draper, R. Ferraz Leal, M. A. Gigg, V. E. Lynch, A. Markvardsen, D. J. Mikkelson, R. L. Mikkelson, R. Miller, K. Palmen, P. Parker, G. Passos, T. G. Perring, P. F. Peterson, S. Ren, M. A. Reuter, A. T. Savici, J.W. Taylor, R. J. Taylor, R. Tolchenov, W. Zhou, and J. Zikovsky, Mantid - data analysis and visualization package for neutron scattering and μ SR experiments, Nucl. Instrum. Methods Phys. Res., Sect. A **764**, 156 (2014).

[34] R. A. Ewings, A. Buts, M. D. Le, J. van Duijn, I. Bustinduy, and T. G. Perring, HORACE: Software for the analysis of data from single crystal spectroscopy experiments at time-of-flight neutron instruments, Nucl. Instrum. Meth. Phys. Res. A **834**, 132 (2016).

[35] S. Toth and B. Lake, Linear spin wave theory for single-Q incommensurate magnetic structures, J. Phys.: Condens. Matter **27**, 166002 (2015).

[36] E. Rastelli, A. Tassi, and L. Reatto, Non-simple magnetic order for simple Hamiltonians, Physica B+C **97**, 1 (1979).

[37] J. B. Fouet, P. Sindzingre, and C. Lhuillier, An investigation of the quantum J_1-J_2-J_3 model on the honeycomb lattice, Eur. Phys. J. B **20**, 241 (2001).

[38] A. R. Wildes, B. Roessli, B. Lebech, and K. W. Godfrey, Spin waves and the critical behaviour of the magnetization in $MnPS_3$, J. Phys.: Condens. Matter **10**, 6417 (1998).

[39] D. Lançon, H. C. Walker, E. Ressouche, B. Ouladdiaf, K. C. Rule, G. J. McIntyre, T. J. Hicks, H. M. Rønnow, and A. R. Wildes, Magnetic structure and magnon dynamics of the quasi-two-dimensional antiferromagnet $FePS_3$, Phys. Rev. B **94**, 214407 (2016).

[40] A. R. Wildes, J. R. Stewart, M. D. Le, R. A. Ewings, K. C. Rule, G. Deng, and K. Anand, Magnetic dynamics of $NiPS_3$, Phys. Rev. B **106**, 174422 (2022).

[41] S. M. Winter, Magnetic couplings in edge-sharing high-spin d^7 compounds, J. Phys. Mater. **5**, 045003 (2022).

[42] H.-J. Koo, R. Kremer, and M.-H. Whangbo, Unusual spin exchanges mediated by the molecular anion $P_2S_6^{4-}$: Theoretical analyses of the magnetic ground states, magnetic anisotropy and spin exchanges of MPS_3 (M = Mn, Fe, Co, Ni), Molecules **26**, 1410 (2021).

[43] G. T. Long and D. A. Cleary, ESR spectroscopy of Co^{2+} impurities in $Cd_2P_2S_6$, and $Cd_2P_2Se_6$, J. Phys.: Condens. Matter **2**, 4747 (1990).

[44] M. A. Hefni, Electronic paramagnetic resonance studies of $CdPS_3 : Co^{2+}$ single crystals, J. Phys. Soc. Jpn. **61**, 2534 (1992).

[45] W.-C. Zheng and S.-Y. Wu, Explanation of the EPR *g* factors for Co^{2+} impurities in trigonal $Cd_2P_2S_6$ crystal, Phys. B: Condens. Matter **307**, 28 (2001).

[46] A. Wildes, B. Fåk, U. B. Hansen, and M. Enderle, The spin wave spectrum of $CoPS_3$ Separation of magnetic and phononic contributions (2020), doi: 10.5291/ILL-DATA.4-01-1651.

[47] A. R. Wildes, J. R. Stewart, B. Fåk, U. B. Hansen, L. Testa, H. M. Rønnow, and J.-G. Park, The spin wave scattering from single crystals of $CoPS_3$ (2020), doi: 10.5286/ISIS.E.RB2010386.